Supplementary Materials for

Active sites in heterogeneous ice nucleation - the example of K-rich feldspars

Alexei Kiselev[1]*, Felix Bachmann[1,3†], Philipp Pedevilla[4], Stephen J. Cox[4], Angelos Michaelides[5], Dagmar Gerthsen[3] and Thomas Leisner[1,2]
correspondence to: alexei.kiselev@kit.edu

This PDF file includes:

Other Supplementary Materials for this manuscript includes the following:

Movies SM1 to SM4

GROMACS structure file of ice on feldspar:
00_minimize_m_100_pris_100_4L_0337.gro

Experimental dataset. Zipped folder “experimental_SM.tar.gz” that contains the original experimental data: ice crystal nucleation map with crystal coordinates from eight nucleation cycles, data used for calculation of on-set supersaturation, wireframes of crystal habits, and original image frames for all figures and supplementary figures recorded with the ESEM.

Computational dataset. Zipped folder “computational_SM.tar.gz” that contains all of our main structures as well as files that contain information about the computational settings used in this work.

Authors contributions

A. K. and T. L. conceived the idea of the experiment. A. K. and F. B. have built the hardware extension of the ESEM, performed the experiments, and analyzed the data with contributions from T. L. and D. G. The atomistic interpretation of the observed phenomena was suggested by P. P., S. J. C., and A. M., who also performed the numerical modelling and contributed to writing the manuscript. T. L. and D. G. supervised the experimental study and helped to write the manuscript. All authors discussed the results and contributed to the final version of manuscript.

Materials and Methods

K-rich feldspar has recently been identified as one of the most active atmospherically relevant IN mineral (*2*) and here we report results on two specimens: orthoclase FSM and microcline FS04. The chemical and mineral compositions of the specimens are given in the Supporting Information (SI, Table ST1). In our recent study (*40*), one of the specimens (FS04) was found to nucleate ice in supercooled droplets already at -5°C. All experiments reported here were conducted in an Environmental Scanning Electron Microscope (ESEM, FEI QUANTA 650 FEG) operated at 10 kV. The instrument is equipped with a custom built temperature controlled specimen holder and gas humidification system (see Fig. S1). By cooling the specimen stage holding a small (approx. 1x1x2 mm) single crystal samples at constant cooling rate (typically 0.6 K/min) and constant vapor pressure in the specimen chamber, the deposition nucleation and growth of individual ice crystals on the samples can be observed, as described e.g. by Zimmermann et al (*50*). To investigate the role of the crystalline substrate we compare ice nucleation on the crystal faces of feldspar with (001) and (010) Miller indices, obtained by mechanical cleavage. In the course of the experiments, we investigated the effect of chemical aging by comparing freshly cleaved fragments of feldspar with fragments that had been placed in carbonated water (pH value in the range from 3 to 5) for several days. We also studied the effects of surface treatment with either 5 wt% aqueous solution of sulphuric acid or 30 wt% aqueous solution of hydrogen peroxide. In all cases the water vapor supersaturation at ice nucleation onset has been determined by analyzing the growth velocity of the individual ice crystals (see section S1 of the Supplementary Material for the detailed procedure).

In addition to the scanning electron microscopy measurements we also performed an extensive set of simulations for water and ice on various feldspar surfaces. Full details are given below in the SM. To summarize, we performed all-atom force field studies of water and ice on feldspar (001), (010), and (100) surfaces using the CLAYFF model (*47*) for feldspar and SPC (*48*) for water. The stoichiometry of our feldspar bulk unit cell was $K_4Al_4Si_{12}O_{32}$ and all our simulations involved slab models of the substrate with periodic boundary conditions. To identify low energy structures we made use of a recently developed structure search method, which has been applied already to water on the (001) surface of feldspar (*43*).

Supplementary Text

S1. ESEM instrument and gas humidification system

All experiments reported here were conducted in an Environmental Scanning Electron Microscope (ESEM, FEI QUANTA 650 FEG) equipped with a custom built temperature controlled specimen holder and gas humidification system. ESEM allows high resolution observation of microscopic objects while maintaining partial water vapor pressure up to 2 kPa in the specimen chamber. Following the approach described by Zimmermann et al. (*50–52*) we control the temperature of the specimen while adjusting the partial vapor pressure in the sample chamber until the vapor saturation value required for nucleation of ice is reached. For this study, the standard cooling stage provided by FEI company was replaced by a double stage Peltier element, thus extending the low temperature limit down to 213K (originally 248K). The hot side of the Peltier element was pressed against a water cooled copper block connected to a chiller through a pair of silicon tubes. The cold side of the Peltier element (5 x 5 mm) served as a cold stage, where the specimen was fixed with a small amount of vacuum grade heat conducting paste. A temperature sensor (Pt-100) was placed near the specimen.

The standard water vapor supply unit of the microscope (capable of providing pure water vapor but not a mixture of gases) has not been used in this work. Instead, we have connected the specimen chamber to a custom built gas humidification (GH) system. A diagram of the GH system is shown in Fig. S1. The working gas mixture was produced by humidifying the nitrogen flow in a Nafion® humidifier (MH-070, PermaPure) that was kept at constant temperature and pressure (typically 300 mbar). After reaching equilibrium conditions in the GH system, the high flow needle valve between the ESEM specimen chamber and GH system was opened to allow the nitrogen - water vapour mixture to fill the specimen chamber to a desired pressure. The pressure in the specimen chamber was monitored continuously by using a pressure transducer connected to the specimen chamber (Fig. S1). As soon as the desired pressure in the specimen chamber was reached, the high flow valve was closed and the fine adjustment of the flow was done with the low flow needle valve. In this way a constant gas flow through the electron beam aperture (500 μm) into the differential pumping system of the ESEM was maintained.

With the total pressure in the GH system P_{GH} and temperature in the humidifier T_{HUM}, the partial water vapour pressure inside the specimen chamber P_{WESEM} can be calculated as:

$$P_{WESEM} = \frac{P_{WGH}\,(T_{HUM})}{P_{GH}} P_{ESEM} \tag{S1}$$

where $P_{WGH}\,(T_{HUM})$ is the saturation pressure of water vapour at the temperature T_{HUM}. The pressure in the GH system P_{GH} was kept typically at 30 kPa and T_{HUM} at 288 K. The total pressure inside the specimen chamber of ESEM was chosen in the range from 100 Pa to 1000 Pa to provide the optimal image quality (in terms of spatial resolution and noise level).

Fig. S1.

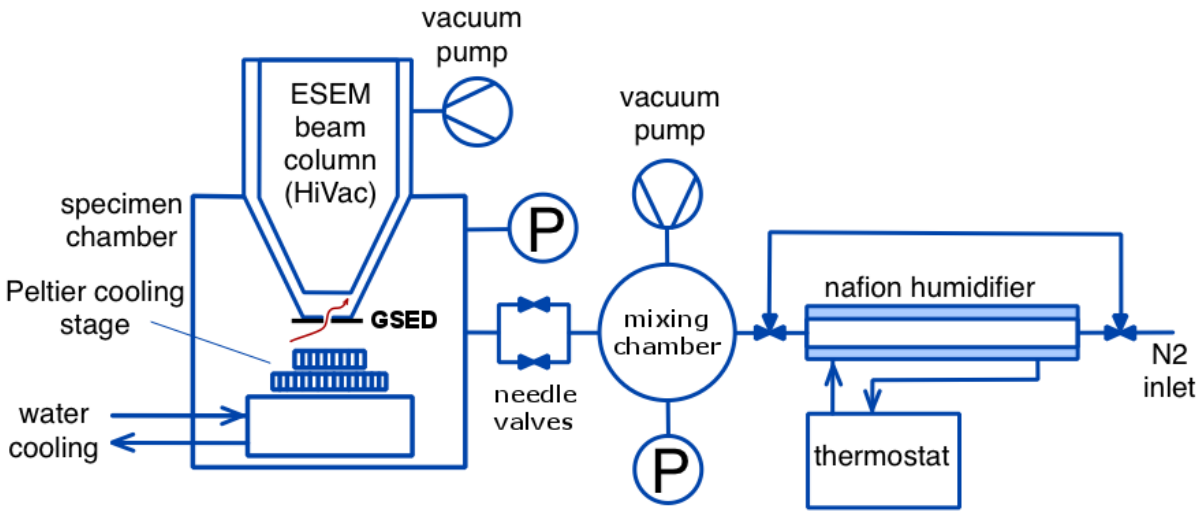

ESEM specimen chamber with gas humidification system. A specimen and the temperature sensor are located on the upper surface of the Peltier stage. The red arrow indicates the gas flow through the 500 µm aperture in the gaseous secondary electron detector (GSED) separating the ESEM chamber from the differential pumping system.

Due to the temporal pressure drop in the GH system during the filling of the specimen chamber, the ratio P_{ESEM}/P_{GH} was not constant with time and therefore the final value of P_{WESEM} was always smaller than predicted (equation S1). For this reason, the supersaturation values at ice nucleation on-set have been determined by measuring the linear growth rates of individual ice crystals, as described in section S3.

S2. Sample preparation

We have used two different samples of the alkali feldspar group (orthoclase and microcline) characterized by general formula $(Na,K)AlSi_3O_8$ with prevailing potassium concentration (*40*). The chemical composition of the specimens, their origin, properties, and notations are summarized in Table S1.

Table S1.

Sample	Abbr.	Source	Number of specimens	Number of experiments*	Mineral composition	Crystal system	Chemical treatment
Orthoclase	FSM	Superior Mine, Houghton Co, Michigan, US	9	15	77% K-feldspar** 23% Na-feldspar**	monoclinic	H_2O+CO_2 H_2SO_4 H_2O_2
Microcline	FS04	Mt. Maloso, Zomba District, Malawi	6	16	80% microcline 18% albite 2% quartz	triclinic	H_2O+CO_2 H_2SO_4 H_2O_2

*) one experiment consists of several nucleation-evaporation cycles

**) mineral phase was evaluated from the Energy Dispersive X-Ray (EDX) spectroscopic measurement of a bulk specimen

Feldspar samples used in the present study

The specimens of FSM (approximately 2×2×1 mm in size) have been prepared by mechanically cleaving the feldspar crystal. The (001) crystalline face of feldspar was identified as the only plane of perfect cleavage. The (010) face is the only plane in feldspar that has a right angle relative to (001) surface and a reasonably good cleavage. The specimens of FS04 have been prepared by cleaving the bulk feldspar monocrystals mechanically and then sawing 1 mm thick slabs parallel to the cleaved surfaces. The orientation of the crystal faces has been confirmed by obtaining the X-ray diffraction patterns in Laue configuration which have been then analysed with CLIP software (*53*). Smaller individual specimens used in the experiments have been broken off the prepared slabs and have been mounted onto the Peltier cooling stage with the cleaved surface facing upwards.

All specimens were investigated either freshly cleaved or aged in room air or distilled water for at least an hour. To enforce the hydroxylation of the feldspar surface we kept some of the specimens in carbonated water, prepared by placing a small chunk of dry ice and small amount of distilled water into a pressurized bottle. At room temperature this results in approximately 1% of dissolved CO_2 which partly reacts with water giving a very weak solution of carbonic acid. In addition, two specimens of FS04 and one specimen of FSM have been treated overnight with a weak aqueous solution (5%w) of H_2SO_4 and then thoroughly rinsed with distilled water. No traces of sulphur have been detected in the EDX spectra of the treated specimens. One specimen of each FSM and FS04 samples has been also treated with 30% aqueous solution of hydrogen peroxide (H_2O_2) at 65°C for one hour, following the procedure described previously (*40*).

Fig. S2.

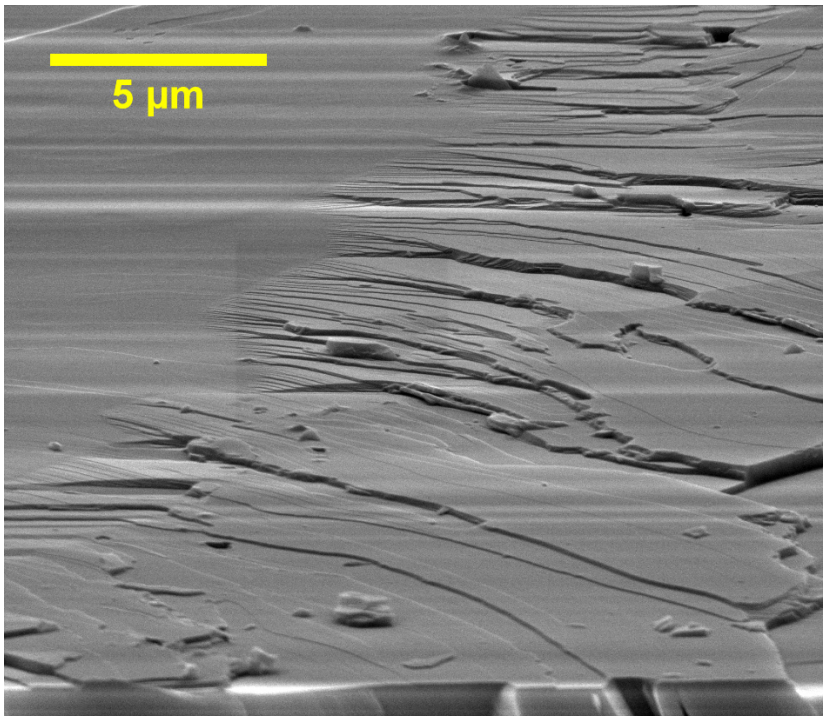

Surface topography of a freshly cleaved (010) face of FSM specimen.

S3. Observation of the ice nucleation and calculation of the ice onset supersaturation

In every experiment the specimen chamber was evacuated to a pressure of 5×10^{-4} Pa before the gas mixture was allowed to enter the specimen chamber until the target frost point was reached. After constant gas flow had been established, the specimen was pre-cooled quickly to a temperature 5K higher than the target frost point and a cooling ramp (typically 0.6 K/min) was initiated. The specimen was cooled until the first ice nucleation event within the field of view (max. 700 µm in diameter) was observed and was then kept at a constant temperature in order to slow down the ice crystal growth. Image frames with a resolution of 1024×943 pixel have been recorded automatically with a rate varying from 0.2 to 1 fps. The temperature on the cold side of the Peltier stage T_S, the total pressure in the specimen chamber P_{ESEM} and the pressure in the gas humidification system P_{GH} have been recorded with 1 s resolution.

As it was not possible to obtain the ice nucleation onset supersaturation σ_0 directly from the pressure measurements, it had to be evaluated from the measurements of the ice crystal growth rates. To do so, we follow the theoretical framework of ice growth kinetic formulated by Yokoyama and Kuroda (*54*) and Libbrecht (*55*, *56*). In this approach, the growth velocity v_n of a solidification front normal to the ice surface can be calculated with

the Hertz-Knudsen equation, originally applied to the adsorption of gas molecules onto the solid substrate (*57*):

$$v_n = \alpha \cdot \frac{c_{sat}}{c_{solid}} \cdot \sqrt{\frac{kT}{2\pi m}} \cdot \sigma_{surf} \tag{S2}$$

where k is the Boltzman constant, T is the gas temperature, m is the mass of a water molecule, $\sigma_{\mathrm{surf}} = (\mathrm{c_{surf}} - \mathrm{c_{sat}})/\mathrm{c_{sat}}$ is the supersaturation of water vapor just above the growing surface, $\mathrm{c_{surf}}$ and $\mathrm{c_{solid}}$ are the number densities of water molecules in gas above the surface and in bulk ice, respectively, and $\mathrm{c_{sat}}$ (T) is the equilibrium number density of water vapor molecules above the flat ice surface. α is a sticking coefficient equal to the probability that a water molecule from the gas phase will be assimilated by the bulk ice on a single collision, and is generally not known a priori. Note that $\alpha = 1$ does not mean that that the molecule is immediately incorporated into the crystal lattice right on the collision spot, it is allowed to move along the ice surface until it becomes incorporated at the most favorable attachment site. Following Libbrecht (*56*) we restrain to the case of finite attachment kinetics $\alpha < 1$ and assume that the growing crystal has a fictitious spherical "faceted" surface characterized by a single value of sticking coefficient α. The latter assumption is valid because ice crystals observed in this study had axis ratios close to one, indicating a similar growth velocity for both basal and prism facets. Furthermore, we take into account that ice crystal is growing on a solid surface, and therefore the latent heat released by ice formation is efficiently transferred into the substrate. With these assumptions, the growth velocity is given by:

$$v_n = \frac{\alpha}{\alpha\,(1+\chi)+\alpha_{diff}} \cdot \frac{c_{sat} D_{FMR} \sigma_0}{c_{solid} \cdot R} \tag{S3}$$

where σ_0 is the supersaturation far from the crystal surface and R is the characteristic crystal radius. For the working pressure in the specimen chamber of 500 Pa the mean free path $\lambda = 13\ \mu m$ is comparable to the size of the small ice crystals and therefore the diffusivity of water vapour D has to be modified to account for transition between continuum and free molecular regime, FMR (*58*):

$$D_{FMR} = \frac{D\,(P_{ESEM})}{\frac{R}{R+\Delta_v} + 4 \cdot \frac{D\,(P_{ESEM})}{\alpha R c_w\,(T_g)}} \tag{S4}$$

Here D is the diffusivity of water vapor at pressure P_{ESEM} in continuum diffusion regime, c_w is the average thermal velocity of water molecules at gas temperature T_g, and Δ_v is the so called *vapor jump length*, or thickness of a layer near the ice surface where diffusion of water vapor cannot be described as continuous (*17*). The jump length is equal to the product of mean free path and the Cunningham correction factor $\Delta_v = \lambda \cdot C_c$. In equation S5, the quantity α_{diff} is introduced to account for pure diffusional growth of ice:

$$\alpha_{diff} = \frac{D_{FMR}}{R} \sqrt{\frac{2\pi m}{kT}}\,, \tag{S5}$$

The heating of ice crystal due to the release of latent heat, together with the heat removal via substrate is described by

$$\chi = \frac{2\,\eta\, D_{FMR}\,\lambda\,\rho_{ice}}{G\kappa_{ice}}\frac{c_{sat}}{c_{solid}} \qquad \text{(S6)}$$

where ρ_{ice} and κ_{ice} are the density and thermal conductivity of ice and $\eta(T) = d\,(\ln\,(c_{sat}(T))/dT$ describes the slope of the curve $c_{sat}\,(T)$. The geometric factor G is unity for the simplified hemispherical shape of hypothetical ice crystal.

Fig. S3.

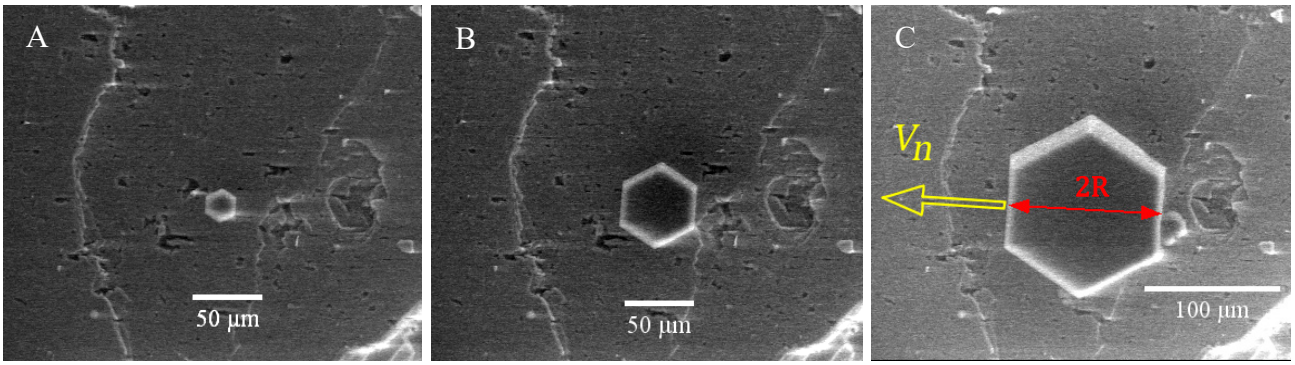

Example ESEM images of an individual ice crystal used for v_n analysis; A) at the moment of detection, B) 10 s later, and C) 35 s after first detection. Red arrow shows the relevant crystal dimension 2R, and the yellow arrow indicates the direction of growth velocity vector.

The growth velocity of ice v_n was estimated from the set of individual ESEM images showing individual crystal with basal or prismatic faces oriented in the plane of image (Fig. S3). It should be noted that the local supersaturation could only be obtained for crystals that nucleated within the field of view, but not for those that grew into that region.

The values of σ_0 were calculated using equation (S3) for all major cases studied in this work (figure S4). The values of σ_0 follow the general trend observed for the lines of constant surface number density of Ice Nucleation Active Sites (INAS) for deposition nucleation on mineral dusts (*5*, *6*). The increase of the nucleation onset supersaturation at low temperatures is in agreement with the classical nucleation theory (CNT) formulation for the deposition nucleation of ice (*59*).

The onset supersaturation obtained in this study are lower than the values for K-rich feldspars obtained in the studies of Yakobi-Hancock et al. (*8*), and Zimmermann et al. (*50*). This is an expected result because the surface area of the macroscopic specimen used in this study is much larger than the total surface area of the individual particles used in the cited works. Within the concept of random distribution of ice active sites, the larger surface is equivalent to a higher probability of having a very effective INAS capable of nucleating ice at low supersaturation.

Fig. S4.

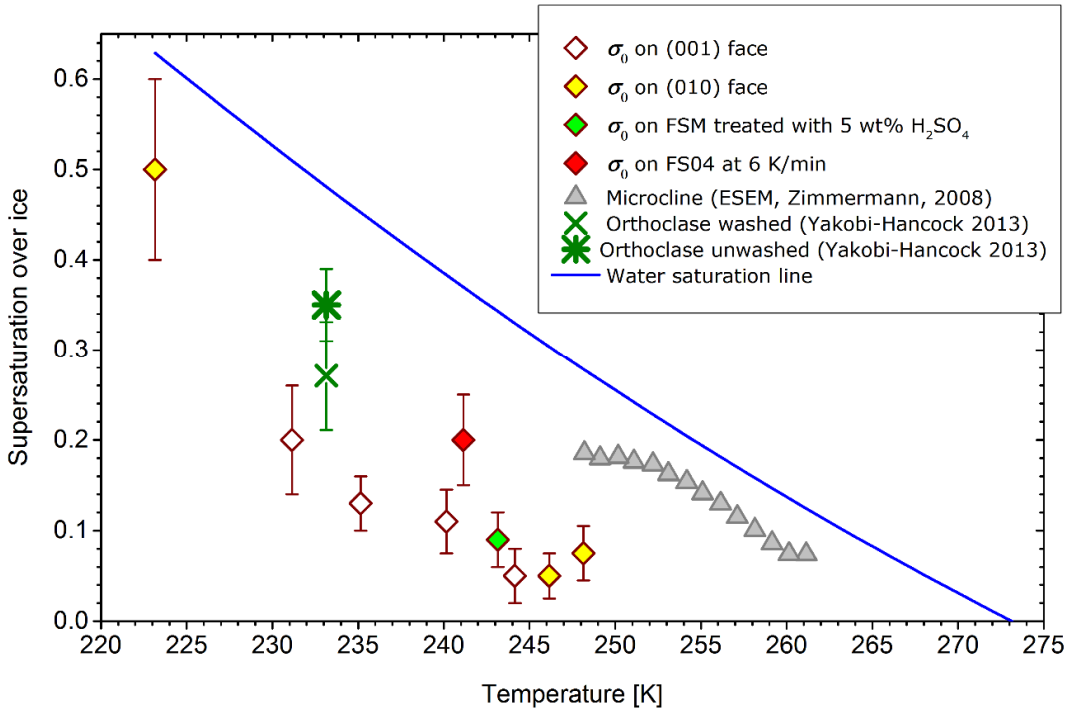

Apparent supersaturation at the ice nucleation on-set σ_0 calculated from the ice crystal linear growth velocity. Red diamond shows the ice onset supersaturation observed for the cooling rate of 6 K/min, as compared to all other cases where cooling rate was kept at 0.6 K/min. Solid blue line is the water vapor saturation with respect to liquid water. For comparison, measurement data of other groups (8, 50) are also shown.

S4. Requirements for ice nucleation in preferential orientation.

Preferential orientation was observed exclusively on the feldspar specimens weathered in the lab air or in the carbonated water for several days, at a temperature down to 230K. On the freshly cleaved faces, ice was nucleating at a much higher supersaturation as an aggregation of tiny crystals "creeping" along the surface of a specimen (Fig. S5a). At lower temperature, ice was nucleating in a random orientation at much higher supersaturation $\sigma_0 = 0.5 \pm 0.1$ (Fig. S5B).

Fig. S5.

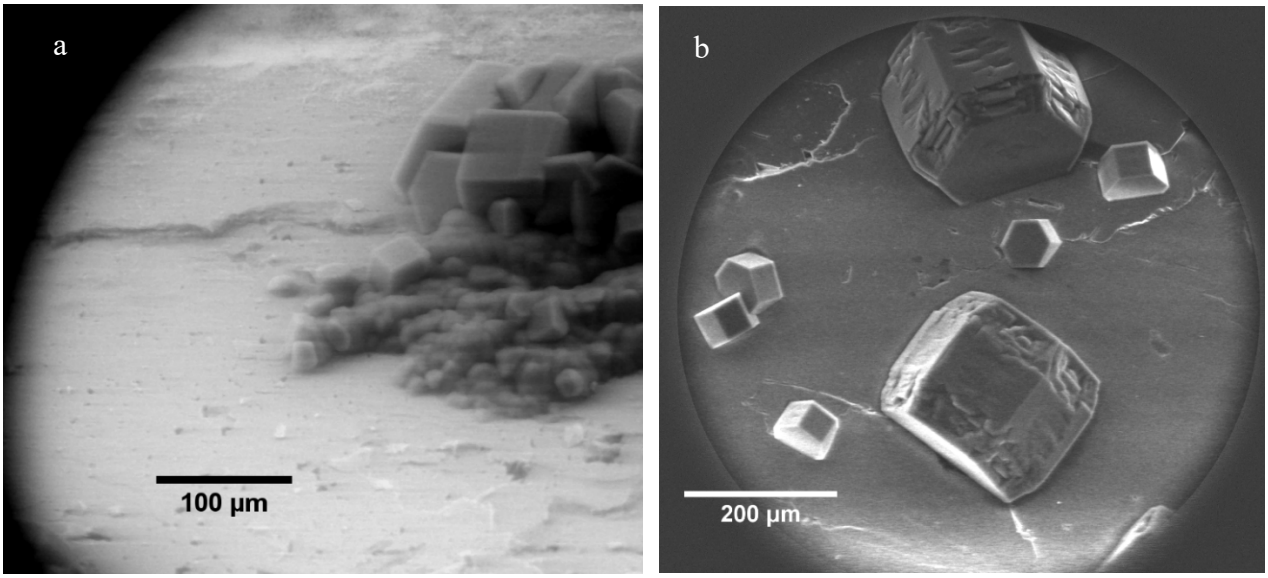

Examples of non-oriented ice growth. a) Creeping ice growing on the surface of freshly cleaved (001) surface of FS04 at 242K and P_{ESEM} = 485 Pa;) random orientation of ice crystals nucleated on the surfaces of FSM at 223K. Cooling rates were 0.6 K/min in both cases.

A second condition for preferential orientation of ice is a low cooling rate (less than 2 K/min). At cooling rates faster than 5 K/min the ice was nucleating at the same sites but had a pronounced polycrystalline character (compare figures S6a and S6b) and the ice nucleation on-set was observed at higher supersaturation, $\sigma_0 = 0.20 \pm 0.07$, whereas only $\sigma_0 = 0.09 \pm 0.06$ was required at 0.6 K/min. As higher supersaturation could be achieved with faster cooling before the nucleation on-set, the growth of ice also becomes faster and the growth mechanism starts being dominated by the attachment kinetics of water molecules(*55*, *60*). In this case the pristine shape of the growing ice crystal cannot develop, resulting in polycrystalline ice.

Fig. S6.

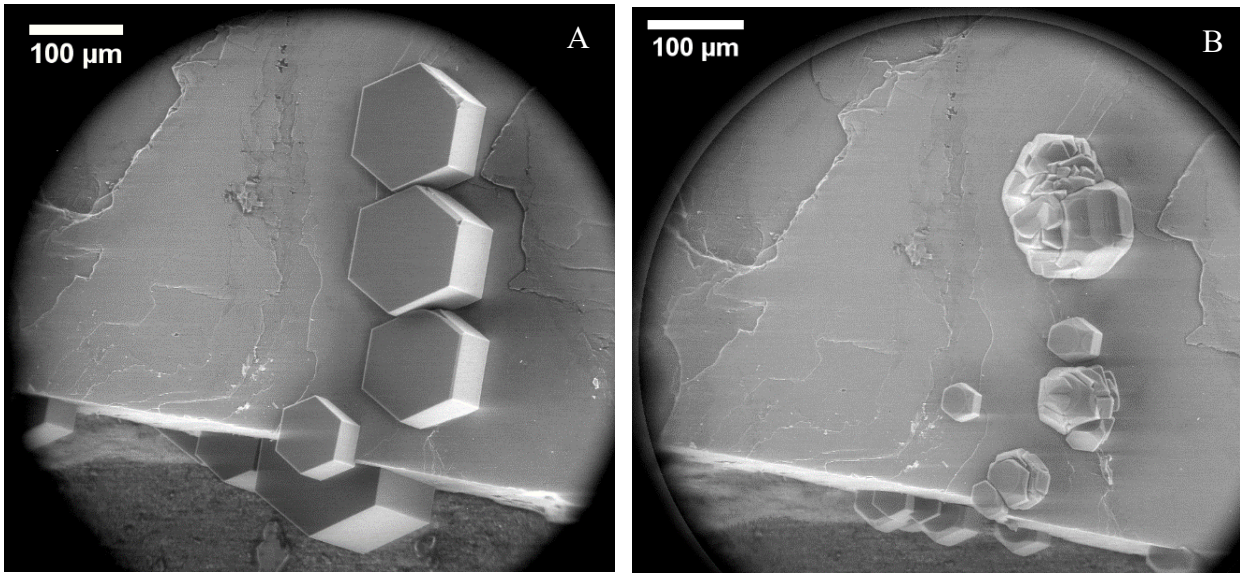

Figure S6. Effect of cooling rate on the shape of ice crystals nucleated on the (001) face of FSM specimen at 241 K and P_{ESEM}=215 Pa. a) Cooling rate 0.6 K/min, b) cooling rate 6 K/min. Note that the preferential nucleation sites are preserved.

S5. Effect of chemical treatment

The preferential orientation on K-rich feldspar can be destroyed by treatment of the specimen in the weak (5 wt%) aqueous solution of sulphuric acid (figure S7a). The on-set of ice crystals nucleation occurred at similar σ_0 (green diamond in the plot of the figure S4). The treatment of feldspar specimens with 30w% aqueous solution of hydrogen peroxide, aimed at the investigation of potential role of biological contamination, did not produce any noticeable effect on the preferential orientation of ice and on the ice on-set supersaturation (Fig. S7b). This is demonstrated in figure S7b, where 25 ice crystals out of 28 within the field of view have identical orientation and tilt.

In our earlier study (*40*), the treatment of FS04 with H_2O_2 has led to deactivation of the high temperature INAS.

Fig. S7.

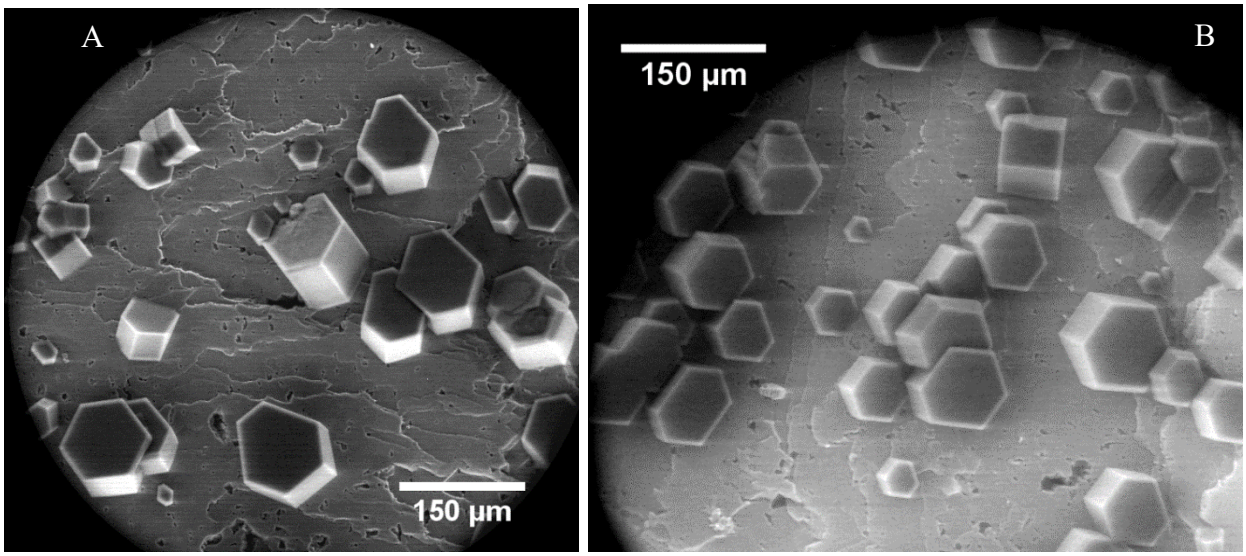

Effect of surface treatment. A) Ice crystals growing in random orientation on the (001) face of FS04 treated by 5w% aqueous solution of H_2SO_4 for several days (T = 242K, P_{ESEM}= 305 Pa). B) Ice crystals growing in the preferential orientation on the face of FS04 specimen treated with H_2O_2 at 60°C for one hour (T = 244K, P_{ESEM}= 400 Pa). Cooling rates were 0.6 K/min in both cases.

Preferential orientation is not observed on freshly cleaved surfaces but only on those aged in weak carbonic acid. Ageing in the aqueous environment leads to the equilibrium configuration of hydroxyl groups, which are assumed to be absent on the freshly cleaved surfaces, providing favorable conditions for ice nucleation in the preferred orientation. Treatment of the feldspar surface with aqueous solution of sulphuric acid modifies this arrangement. Note, however, that we have not observed increase of the ice on-set supersaturation associated with the deactivation of INAS, as reported recently in Sihvonen et al (*61*). This implies that the overall IN efficacy of the patches is not affected, but the condition for preferential orientation is cancelled.

S6. Possible combinations of crystalline planes in ice and feldspar that would explain the observed orientation of ice crystals

From a purely geometrical point of view, the observed tilt and orientation of ice crystals can be explained by nucleation of ice from the primary or secondary prism plane on one of three crystal faces of feldspar, as illustrated in Figure S8. This consideration, however, does not take into account the strong lattice mismatch between orthogonal lattice of ice and triclinic lattice of feldspar for crystals B and C. The origin of this mismatch is discussed in detail in the following section.

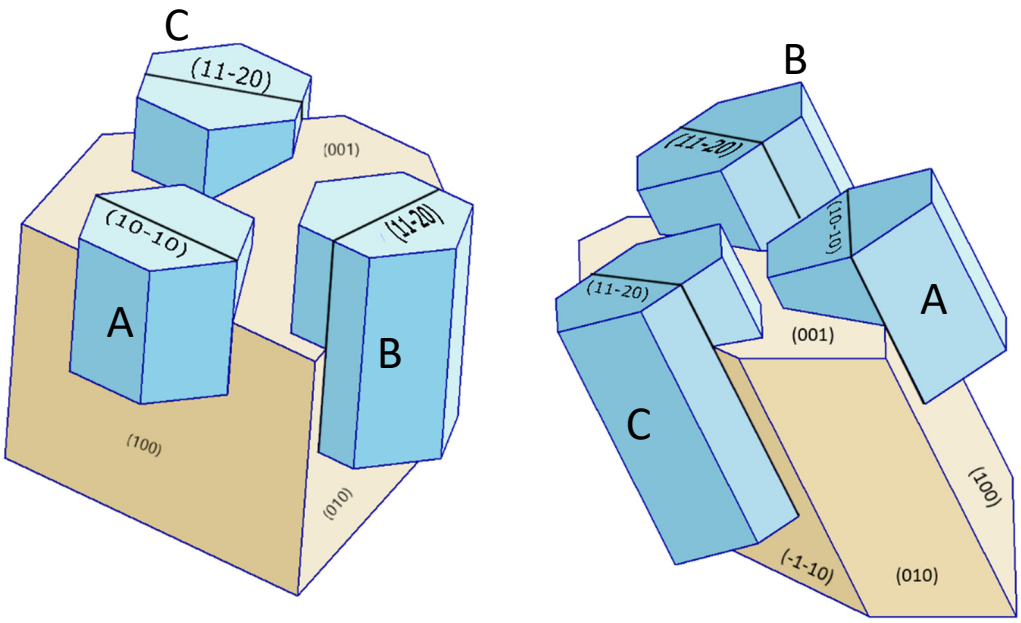

Figure S8. Two different views onto the feldspar specimen with ice crystals, showing various combination of crystal planes in ice and feldspar that would explain the observed relative orientation of ice crystals relative to feldspar specimen. Note that notation $(\bar{1}\bar{1}0)$ *is equivalent to (-1-10),* $(10\bar{1}0)$ *is equivalent to (10-10), and* $(11\bar{2}0)$ *to (11-20).*

Ice crystal A: Ice crystal growing with its $(10\bar{1}0)$ *crystal plane aligned to the (100) face of feldspar.*

Ice crystal B: Ice crystal growing with its $(11\bar{2}0)$ *crystal plane aligned to the (010) face of feldspar.*

Ice crystal C: Ice crystal growing with its $(11\bar{2}0)$ *crystal plane aligned to the* $(\bar{1}\bar{1}0)$ *face of feldspar.*

All three crystals have the same orientation and tilt within the coordinate system associated with primitive unit cell of feldspar. Black lines indicate the cross section of the nucleation crystal plane of ice with the external surfaces of hexagonal prisms. The drawings have been generated with the Shape software (http://www.shapesoftware.com).

S7. K-Feldspar / ice interface structure search

To explore the interfaces between K-feldspar (microcline) and ice we employed a previously developed structure search approach (*43*) based on classical force fields: ClayFF (*47*) to describe microcline and SPC (*48*) to describe water. All energy minimizations were performed using GROMACS (*62*, *63*). Feldspar interfaces were generated by cleaving a highly ordered bulk structure (all Al occupying T_1 sites) of microcline obtained in a previous study (*43*). In the resulting surface slabs, Si/Al tetrahedra that were linked to the framework by only one bridging oxygen atom were removed from the structure, as they are very prone to dissolution. The broken bonds on the surfaces were subsequently saturated by dissociating water molecules (OH and H fragments) to fully hydroxylate undercoodinated Al/Si tetrahedra, as is usually done (*64*). To model different ice surfaces, lattices with constituting lattice points representing the ideal water location in ice I_h for the

basal, primary and secondary prism faces were built. O-O distances and O-O-O angles in these lattices were chosen to be 2.7 Å and 109.47° respectively. To make the unit cells of different ice lattices commensurate with the feldspar lattice, they were scaled isotropically to obtain a uniform distribution of lattice points. Ice lattice sizes were chosen in such a way that they fit onto the microcline surfaces with water densities similar to that of ice. Furthermore, to make sure the cut-offs in the force field can be set to reasonable values (10 Å), we performed the force field minimization not in the primitive unit cell of feldspar, but in larger supercells with comparable dimensions in x and y. The resulting slab models had unit cell sizes (a × b) of approximately 26.2 Å × 22.0 Å ((100) surface), 26.1 Å × 29.2 Å ((010) surface) and 30.9 Å × 29.3 Å ((110) surface).

To then explore the configuration space of different ice faces on different feldspar surfaces, we placed water molecules into the ice lattice sites with a random (uniform) rotational orientation. The centre of mass x and y coordinates of the entire ice lattice as well as its height in z was decided randomly (uniformly). This ensures a reasonable sampling of the configurational space, but at the same time focusing on ice-like structures.

A total of 9 distinct interfaces, coming from a combination of one of the three feldspar surfaces [(100), (010) or (110)] with one of the three faces of ice [(0001), $(10\bar{1}0)$, $(11\bar{2}0)$] have been investigated. For the initial interface structure search, two-layer thick ice faces were considered, and a total of 5000 structure minimizations were performed for each individual interface. For the feldspar (100) / ice $(10\bar{1}0)$ interface, an additional 1000 structure searches were performed using a four-layer thick ice surface to test the reliability of our results.

The results are shown in figure S9. The structure of ice I_h and different feldspar surfaces are shown in rows, different ice surfaces in columns. The three feldspar-ice combinations that could potentially explain the tilt of 26 degrees of the basal plane relative to the feldspar (001) surface are highlighted in green boxes. By visual inspection it becomes clear, that most interfaces identified do not resemble the structure. Nevertheless, one interface in figure S9 stands out as particularly ice-like, namely the primary prism face on feldspar (100). Interestingly, this interface would also explain the experimental observations. The feldspar (010) and feldspar (110) are unlikely candidates to explain the observed tilt, because they do not resemble the structure of ice. The reason behind this is the intrinsic mismatch between the feldspar and ice lattice for the former two cases. Both, the primary and secondary prism faces have an orthogonal lattice (α=90°), whilst the feldspar lattice on all three surfaces is tilted (α ≠ 90°) due to the triclinic unit cell of microcline. None of these interfaces have a perfect lattice match therefore. Whereas this mismatch between ice and feldspar is very pronounced for the (010) surface (α=116°) and the (110) surface (α=103°), it is only very small for the (100) surface (α=91°). Prismatic ice growing on the (100) surface of microcline will therefore be strained to only a small extent and can adapt an ice like structure. In contrast, ice growing on either (010) or (110) will have to adapt to the underlying feldspar substrate and as a result deviate from the ideal ice structure, as the structure search confirms.

To show, that the feldspar (100) / ice $(10\bar{1}0)$ interface not only looks ice like, but also is stable, we calculate its adsorption energy according to:

$$E_{ads} = (E_{interface} - E_{(100)} - nE_{H2O}) / n \quad \text{(S7)}$$

where $E_{interface}$, $E_{(100)}$ and E_{H2O} stand for the total energy of the interface, the total energy of an isolated feldspar (100) slab and the total energy of an isolated water molecule respectively. n stands for the number of water molecules of the interface. The adsorption energy of the most stable four-layer thick primary prism face ice structure on microcline (100) is -0.58 eV/H_2O, which agrees well with typical adsorption energies of water on minerals which are in the range from -0.5 to -0.7 eV/H_2O (*30*, *43*).

Fig. S9.

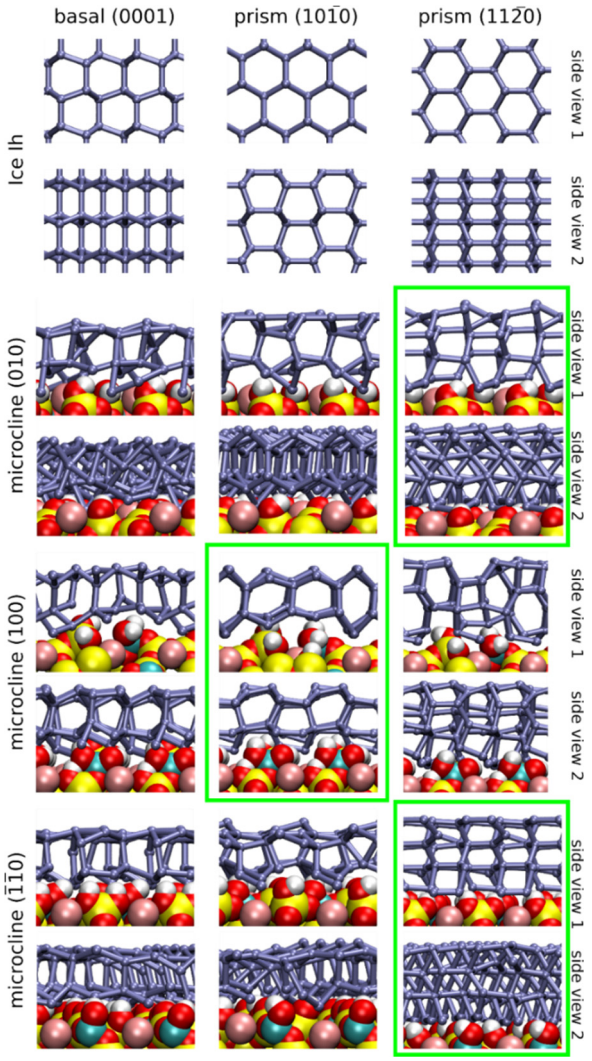

Most stable feldspar/ice interface found for each combination of microcline and ice structure. The first row shows the surfaces of ice Ih that were considered. Side view 1 and 2 have a 90° angle between them in all cases. Ice-like structures on feldspar need to resemble the structures of ice Ih shown in the top row, which is only the case for the primary prism face of ice on microcline (100). The interfaces highlighted in green could potentially explain the experimentally observed tilt of the basal face relative to the feldspar (001) surface. For clarity, only the oxygen atom of water molecules is shown. Furthermore, hydrogen bonded water molecules are connected with a solid metallic blue line.

Supplementary references

1. T. W. Wilson *et al.*, A marine biogenic source of atmospheric ice-nucleating particles. *Nature*. **525**, 234–238 (2015).

2. J. D. Atkinson *et al.*, The importance of feldspar for ice nucleation by mineral dust in mixed-phase clouds. *Nature*. **498**, 355–8 (2013).

3. N. Hiranuma *et al.*, Ice nucleation by cellulose and its potential contribution to ice formation in clouds. *Nat. Geosci.* **8**, 273–277 (2015).

4. M. A. Freedman, Potential Sites for Ice Nucleation on Aluminosilicate Clay Minerals and Related Materials. *J. Phys. Chem. Lett.* **6**, 3850–3858 (2015).

5. N. Hiranuma *et al.*, A comprehensive parameterization of heterogeneous ice nucleation of dust surrogate: laboratory study with hematite particles and its application to atmospheric models. *Atmos. Chem. Phys.* **14**, 13145–13158 (2014).

6. C. Hoose, O. Möhler, Heterogeneous ice nucleation on atmospheric aerosols: a review of results from laboratory experiments. *Atmos. Chem. Phys.* **12**, 9817–9854 (2012).

7. B. J. Murray, D. O'Sullivan, J. D. Atkinson, M. E. Webb, Ice nucleation by particles immersed in supercooled cloud droplets. *Chem. Soc. Rev.* **41**, 6519 (2012).

8. J. D. Yakobi-Hancock, L. A. Ladino, J. P. D. Abbatt, Feldspar minerals as efficient deposition ice nuclei. *Atmos. Chem. Phys.* **13**, 11175–11185 (2013).

9. G. P. Schill, K. Genareau, M. A. Tolbert, Deposition and immersion-mode nucleation of ice by three distinct samples of volcanic ash. *Atmos. Chem. Phys.* **15**, 7523–7536 (2015).

10. A. D. Harrison *et al.*, Not all feldspar is equal: a survey of ice nucleating properties across the feldspar group of minerals. *Atmos. Chem. Phys.* **16**, 10927–10940 (2016).

11. A. Hodgson, S. Haq, Water adsorption and the wetting of metal surfaces. *Surf. Sci. Rep.* **64**, 381–451 (2009).

12. J. Carrasco, A. Hodgson, A. Michaelides, A molecular perspective of water at metal interfaces. *Nat. Mater.* **11**, 667–674 (2012).

13. N. H. Fletcher, Active Sites and Ice Crystal Nucleation. *J. Atmos. Sci.* **26**, 1266–1271 (1969).

14. N. H. Fletcher, Nucleation and Growth of Ice Crystals Upon Crystalline Substrates. *Aust. J. Phys.* **13**, 408 (1960).

15. P. J. Connolly *et al.*, Studies of heterogeneous freezing by three different desert dust samples. *Atmos. Chem. Phys.* **9**, 2805–2824 (2009).

16. W. Cantrell, A. Heymsfield, Production of Ice in Tropospheric Clouds: A Review. *Bull. Am. Meteorol. Soc.* **86**, 795–807 (2005).

17. H. R. Pruppacher, J. D. Klett, *Microphysics of clouds and precipitation* (Kluwer Academic Publishers, 2nd rev. a., 2004).

18. G. Vali, Ice Nucleation Theory. *Molecules*. **1999**, 1–22 (1999).

19. S. J. Cox, Z. Raza, S. M. Kathmann, B. Slater, A. Michaelides, The microscopic features of heterogeneous ice nucleation may affect the macroscopic morphology of atmospheric ice crystals. *Faraday Discuss.* **167**, 389 (2013).

20. M. Fitzner, G. C. Sosso, S. J. Cox, A. Michaelides, The Many Faces of Heterogeneous Ice Nucleation: Interplay between Surface Morphology and Hydrophobicity. *J. Am. Chem. Soc.* **137**, 13658–13669 (2015).

21. G. W. Bryant, J. Hallett, B. J. Mason, The epitaxial growth of ice on single-crystalline substrates. *J. Phys. Chem. Solids*. **12**, 189–IN18 (1959).

22. J. L. Caslavsky, K. Vedam, Epitaxial growth of ice crystals on the muscovite cleavage plane and their relation to partial dislocations. *J. Appl. Phys.* **42**, 516–520 (1971).

23. N. Cho, J. Hallett, Epitaxial ice crystal growth on covellite (CuS) I. Influence of misfit strain on the growth of non-thickening crystals. *J. Cryst. Growth*. **69**, 317–324 (1984).

24. T. Kobayashi, The Growth of Ice Crystals on Covellite and Lead Iodide Surfaces. *Contrib. from Inst. Low Temp. Sci.* **692**, 1–22 (1965).

25. B. Vonnegut, The nucleation of ice formation by silver iodide. *J. Appl. Phys.* **18**, 593–595 (1947).

26. D. Turnbull, B. Vonnegut, Nucleation Catalysis. *Ind. Eng. Chem.* **44**, 1292–1298 (1952).

27. T. Croteau, a. K. Bertram, G. N. Patey, Adsorption and structure of water on kaolinite surfaces: Possible insight into ice nucleation from grand canonical Monte Carlo calculations. *J. Phys. Chem. A*. **112**, 10708–10712 (2008).

28. T. Croteau, A. K. Bertram, G. N. Patey, Simulation of water adsorption on kaolinite under atmospheric conditions. *J. Phys. Chem. A*. **113**, 7826–7833 (2009).

29. X. L. Hu, A. Michaelides, Ice formation on kaolinite: Lattice match or amphoterism? *Surf. Sci.* **601**, 5378–5381 (2007).

30. X. L. Hu, A. Michaelides, Water on the hydroxylated (0 0 1) surface of kaolinite: From monomer adsorption to a flat 2D wetting layer. *Surf. Sci.* **602**, 960–974 (2008).

31. S. A. Zielke, A. K. Bertram, G. N. Patey, Simulations of Ice Nucleation by Kaolinite (001) with Rigid and Flexible Surfaces. *J. Phys. Chem. B*. **120**, 1726–1734 (2016).

32. H. K. Christenson, Two-step crystal nucleation via capillary condensation. *CrystEngComm*. **15**, 2030 (2013).

33. C. Marcolli, Deposition nucleation viewed as homogeneous or immersion freezing in pores and cavities. *Atmos. Chem. Phys.* **14**, 2071–2104 (2014).

34. V. B. Federer, Ueber den Einfluss der Oberflaecheneigenschaften von Halbleitern auf ihre Eiskeimfaehigkeit. *Z. Angew. Math. Phys*. **19**, 378–390 (1968).

35. J. Hallett, S. K. Shrivastava, Nucleation of supercooled water by large single crystals of silver iodide. *J. Rech. Atmos.* **5**, 223–236 (1973).

36. B. J. Anderson, J. Hallett, Supersaturation and Time Dependence of Ice Nucleation from the Vapor on Single Crystal Substrates. *J. Atmos. Sci.* **33** (1976), pp. 822–832.

37. S. J. Cox, S. M. Kathmann, J. a. Purton, M. J. Gillan, A. Michaelides, Non-hexagonal ice at hexagonal surfaces: the role of lattice mismatch. *Phys. Chem. Chem. Phys.* **14**, 7944 (2012).

38. L. Lupi, V. Molinero, Does Hydrophilicity of Carbon Particles Improve Their Ice Nucleation. *J. Phys. Chem. A* (2014), doi:10.1021/jp4118375.

39. L. Lupi, A. Hudait, V. Molinero, Heterogeneous nucleation of ice on carbon surfaces. *J. Am. Chem. Soc.* **136**, 3156–3164 (2014).

40. A. Peckhaus, A. Kiselev, T. Hiron, M. Ebert, T. Leisner, A comparative study of K-rich and Na/Ca-rich feldspar ice nucleating particles in a nanoliter droplet freezing assay. *Atmos. Chem. Phys.* **16**, 11477–11496 (2016).

41. J. V. Smith, *Feldspar Minerals 2 Chemical and Textural Properties* (Springer Berlin Heidelberg, ed. 1, 1974).

42. K. G. Libbrecht, On the Equilibrium Shape of an Ice Crystal. *Proc. R. Soc. London*. **49**, 323–343 (2012).

43. P. Pedevilla, S. J. Cox, B. Slater, A. Michaelides, Can Ice-Like Structures Form on Non-Ice-Like Substrates? The Example of the K-feldspar Microcline. *J. Phys. Chem. C*. **120**, 6704–6713 (2016).

44. I. Parsons, Ed., *Feldspars and Their Reactions* (Kluwer Academic Publishers, Series C:, 1994), vol. 421.

45. J. V Smith, Atmospheric weathering and silica-coated feldspar: analogy with zeolite molecular sieves, granite weathering, soil formation, ornamental slabs, and ceramics. *Proc. Natl. Acad. Sci. U. S. A.* **95**, 3366–3369 (1998).

46. H. Behrens, An Infrared Spectroscopic Study of Hydrogen Feldspar (HA1Si3O8). *Mineral. Mag.* **59**, 15–24 (1995).

47. R. T. Cygan, J.-J. Liang, A. G. Kalinichev, Molecular Models of Hydroxide, Oxyhydroxide, and Clay Phases and the Development of a General Force Field. *J. Phys. Chem. B*. **108**, 1255–1266 (2004).

48. H. J. C. Berendsen, J. P. M. Postma, W. F. van Gunsteren, J. Hermans, Interaction models for water in relation to protein hydration. *Intermol. Forces*, 331–342 (1981).

49. N. Fukuta, B. . Mason, Epitaxial growth of ice on organic crystals. *J. Phys. Chem. Solids*. **24**, 715–718 (1963).

50. F. Zimmermann *et al.*, Ice nucleation properties of the most abundant mineral dust phases. *J. Geophys. Res.* **113**, D23204 (2008).

51. M. Ebert, M. Inerle-Hof, S. Weinbruch, Environmental scanning electron microscopy as a new technique to determine the hygroscopic behaviour of individual aerosol particles. *Atmos. Environ.* **36**, 5909–5916 (2002).

52. F. Zimmermann, M. Ebert, A. Worringen, L. Schütz, S. Weinbruch, Environmental scanning electron microscopy (ESEM) as a new technique to determine the ice nucleation capability of individual atmospheric aerosol particles. *Atmos. Environ.* **41**, 8219–8227 (2007).

53. O. J. Schumann, Cologne Laue Indexation Program, (available at http://clip4.sourceforge.net).

54. E. Yokoyama, T. Kuroda, Pattern formation in growth of snow crystals occurring in the surface kinetic process and the diffusion process. *Phys. Rev. A*. **41**, 2038–2049 (1990).

55. K. G. Libbrecht, The physics of snow crystals. *Reports Prog. Phys.* **68**, 855–895 (2005).

56. K. G. Libbrecht, Growth rates of the principal facets of ice between -10C and -40C. *J. Cryst. Growth*. **247**, 530–540 (2003).

57. K. W. Kolasinski, *Surface Science: Foundations of Catalysis and Nanoscience* (John Wiley & Sons, Ltd, Third edit., 2012).

58. P. V. Hobbs, *Ice Physics* (Oxford University Press, New York, 2010).

59. C. Hoose, O. Möhler, Heterogeneous ice nucleation on atmospheric aerosols: a review of results from laboratory experiments. *Atmos. Chem. Phys.* **12**, 9817–9854 (2012).

60. K. G. Libbrecht, A Critical Look at Ice Crystal Growth Data. *eprint arXiv:cond-mat/0411662*, 21 (2004).

61. S. K. Sihvonen *et al.*, Chemical and physical transformations of aluminosilicate clay minerals due to Acid treatment and consequences for heterogeneous ice nucleation. *J. Phys. Chem. A*. **118**, 8787–96 (2014).

62. D. Van Der Spoel *et al.*, GROMACS: fast, flexible, and free. *J. Comput. Chem.* **26**, 1701–1718 (2005).

63. B. Hess, C. Kutzner, D. Van Der Spoel, E. Lindahl, GRGMACS 4: Algorithms for highly efficient, load-balanced, and scalable molecular simulation. *J. Chem. Theory Comput.* **4**, 435–447 (2008).

64. S. Kerisit, C. Liu, E. S. Ilton, Molecular dynamics simulations of the orthoclase (001)- and (010)-water interfaces. *Geochim. Cosmochim. Acta*. **72**, 1481–1497 (2008).

Supplementary movie captions

Movie SM1

Movie of ice nucleation on the surface of orthoclase (FSM) at 233 K (first nucleation cycle, the end of the movie corresponds to the image in the figure 2B). The field of view is approximately 500 μm wide.

Movie SM2

Movie of oriented ice growth on (001) face of the FS04 specimen at 248 K. The field of view is approximately 500 μm wide.

Movie SM3

Movie of co-aligned ice growth on both (001) and (010) faces of the orthoclase (FSM) specimen at 248 K. The field of view is approximately 500 μm wide.

Movie SM4

Zoom onto the first nucleation event of the nucleation cycle from the movie S1. The horizontal dimension of the frame is approximately 15 μm.